Monitoring of the central blood pressure waveform via a conformal ultrasonic device

Chonghe Wang[#1], **Xiaoshi Li**[#2], **Hongjie Hu**[#2], **Lin Zhang**[1], **Zhenlong Huang**[1], **Muyang Lin**[7], **Zhuorui Zhang**[1], **Zhenan Yin**[3], **Brady Huang**[5], **Hua Gong**[1], **Shubha Bhaskaran**[3], **Yue Gu**[2], **Mitsutoshi Makihata**[6], **Yuxuan Guo**[1], **Yusheng Lei**[1], **Yimu Chen**[1], **Chunfeng Wang**[8], **Yang Li**[1], **Tianjiao Zhang**[1], **Zeyu Chen**[4], **Albert Pisano**[6], **Liangfang Zhang**[1], **Qifa Zhou**[4], and **Sheng Xu**[1,2,3,9,*]

[1]Department of Nanoengineering, University of California San Diego, La Jolla, CA, 92093-0448, USA.

[2]Materials Science and Engineering Program, University of California San Diego, La Jolla, CA, 92093-0418, USA.

[3]Department of Electrical and Computer Engineering, University of California San Diego, La Jolla, CA, 92093-0407, USA.

[4]Department of Ophthalmology and Biomedical Engineering, Viterbi School of Engineering, University of Southern California, Los Angeles, CA 90089-1111, USA.

[5]Department of Radiology, School of Medicine, University of California San Diego, La Jolla, CA, 92103, USA.

[6]Department of Mechanical and Aerospace Engineering, University of California San Diego, La Jolla, CA, 92093-0411, USA.

[7]School of Precision Instrument and Optoelectronic Engineering, Tianjin University, Tianjin, 300072, China.

[8]The Key Laboratory of Materials Processing and Mold of Ministry of Education, School of Materials Science and Engineering, School of Physics & Engineering, Zhengzhou University, Zhengzhou, 450001, Henan, China.

[9]Department of Bioengineering, University of California San Diego, La Jolla, CA, 92093-0412, USA.

*Corresponding author. shengxu@ucsd.edu.
Correspondence and requests for materials should be addressed to S.X.

# These authors contributed equally to this work.

Abstract

Continuous monitoring of the central-blood-pressure waveform from deeply embedded vessels, such as the carotid artery and jugular vein, has clinical value for the prediction of all-cause cardiovascular mortality. However, existing non-invasive approaches, including photoplethysmography and tonometry, only enable access to the superficial peripheral vasculature. Although current ultrasonic technologies allow non-invasive deep-tissue observation, unstable coupling with the tissue surface resulting from the bulkiness and rigidity of conventional ultrasound probes introduces usability constraints. Here, we describe the design and operation of an ultrasonic device that is conformal to the skin and capable of capturing blood-pressure waveforms at deeply embedded arterial and venous sites. The wearable device is ultrathin (240 μm) and stretchable (with strains up to 60%), and enables the non-invasive, continuous and accurate monitoring of cardiovascular events from multiple body locations, which should facilitate its use in a variety of clinical environments.

The variation of blood-pressure (BP) waveforms contains abundant information of the dynamic cardiovascular status[1,2]. Each one of peaks and notches in the arterial BP waveform represents a specific left heart activity. Likewise, the characteristic morphology of the venous BP waveform is closely related to relevant right heart events[3]. Therefore, continuous monitoring of subtle changes of those vital signals can provide remarkable insights for cardiovascular disease diagnosis and prognosis[4]. Although monitoring the vascular pulsation at the peripheral sites is useful for specific symptoms, emerging evidence suggests that the central arterial and venous BP waveforms possess significantly more relevance to cardiovascular events than the peripheral BP (PBP)[5–8]. Firstly, major organs, including the heart, kidneys, lungs, and the brain, are directly exposed to the central arteries. Therefore the distending pressure in the large elastic arteries (such as aorta and carotid) is a vital determinant of the degenerative changes that characterize accelerated aging and hypertension[9]. Secondly, amplification and reflection effect caused by the complexities of peripheral vascular resistance along the conduit artery, namely the stiffness mismatch between the peripheral and central vessels, is tough to evaluate. This uncertainty often creates irregular and unpredictable influence on the PBP waveform, making it incapable of achieving reliable cardiovascular status assessment[10]. Thirdly, although the central-blood-pressure (CBP) waveform can sometimes be derived from the PBP waveform by the translational equation, demographic results indicate that clinical treatment, such as using BP lowering drugs, can exert different effects on PBP and CBP waveforms[7,11], causing inaccurate recordings[12]. Such inaccuracy can cause errors in the assessment of myocardial oxygen requirements[13] and ventricular load and hypertrophy[14], as well as disparities in the actions of different vasodilator agents[15]. Therefore, treatment decisions for cardiovascular diseases should be based on CBP rather than PBP waveforms[16].

The gold standard for recording the CBP waveforms in the carotid artery and jugular venous sites, cardiac catheterization (also known as cannulation), involves implanting a fiber-based pressure sensor into the relevant vasculature[17] (Supplementary note 1). Despite its high accuracy, it causes patient suffering and increases the risk of infection, and thus is too

invasive for routine inspections[1]. Although there are several non-invasive methods including the optical method (photoplethysmography (PPG), or volume clamp)[18], tonometry[4,19], and ultrasound wall-tracking that can potentially monitor the CBP waveform, they suffer from several technical challenges. Specifically, the PPG has insufficient penetration depth (<8 mm) for measuring central vasculature which is often embedded in the tissue thickness > 3 cm[20]. Other technical problems of PPG can be summarized as signal aliasing from venous and arterial pulsations[21], susceptibility to heat, moisture[22], and high dependence on constant blood constituent[23]. The tonometry involves using strain sensors to detect the vessel pulsation. This method highly relies on the efficiency of the blood vessel flattening by the tonometer. Therefore, this is only recommended for the PBP measurement where a supporting bony structure is available, which can provide a solid mechanical support[24]. Due to this reason, its accuracy largely degrades for measuring central vasculatures that have no proximal supporting skeletons. Also, this method is susceptible to the subject's obesity that highly dampens the pulse wave propagation (Supplementary notes 2 and 3; Supplementary Figs. 1 and 2). With the high penetrating capability, the ultrasound wall-tracking technique utilizes the high-speed imaging probe to track the pulsation of the vasculature embedded in deep tissues[25]. However, the imaging probe is highly sensitive to motion artifacts, which will bring significant burden to its associated wall-tracking recognition algorithm (Supplementary note 4; Supplementary Fig. 3). Additionally, current ultrasound imaging probes are heavy and bulky. A reliable acoustic coupling interface requires a stable holding of the probe by the operator. This will introduce an inevitable compression of local vasculatures, which will change their distending behavior and lead to inaccurate recordings (Supplementary Fig. 4). Therefore, this method is not suitable for long-term monitoring purposes.

Wearable devices with the compliant mechanical properties similar to the skin offer the capability of non-invasive, continuous monitoring of a variety of vital signs[26], such as local field potentials[27], temperature[28], sweat content[29,30], and skin hydration[31]. However, their applications have typically been limited to recording signals on the skin or shallow tissue underneath the epidermis. Here, we introduce an approach that allows integrating ultrasonic technology on the wearable system. The ultrasonic waves can effectively penetrate the human tissues up to 4 cm, which opens up a third dimension to the sensing range of current state-of-the-art wearable electronics. With similar mechanical properties to the skin and an ultrathin profile, the wearable ultrasonic device can ensure a conformal intimate contact to the curvilinear and time-dynamic skin surface, and continuously monitor CBP of deep vasculatures without the operational difficulties or instabilities in the other conventional approaches. This capability of non-invasive, continuous, and accurate monitoring of deep biological tissues/organs opens up opportunities for diagnosing and predicting a broad range of cardiovascular diseases in a wearable format.

Results:

Device design and working principle.

The device hybridizes high performance rigid 1–3 piezoelectric composites with soft structural components (Fig. 1a and Supplementary Figs. 5 and 6). The anisotropic 1–3

composite possesses better acoustic coupling with soft biological tissue than isotropic piezoelectric materials. By balancing geometrical and electrical designs, our device can reach an ultrathin thickness (240 μm, three orders of magnitude thinner than existing medical ultrasonic probes) (Supplementary note 5). The elastic and failure strain levels are up to 30% and 60%, respectively (Supplementary Figs. 7 and 8). The functional material used in this study, 1–3 piezoelectric composite with a thickness of 200 μm, has a working frequency of 7.5 MHz (Supplementary Fig. 9). This material selection enables a 400 μm axial resolution (Methods section and Supplementary Fig. 10) that is comparable with available medical ultrasonic probes at the same working frequency. The 1–3 composite has piezoelectric micro-rods embedded, in a periodic configuration in a passive epoxy matrix, which substantially increases the longitudinal coupling coefficient k_{33} by suppressing the shear vibrating modes. The rigid piezoelectric transducer element is diced to have 0.9*0.9 mm^2 footprint to allow sufficient penetration depth into the tissue, and also has minimal mechanical loading to the entire device (Fig. 1b).

Bilayer stacking of polyimide (PI, 4 μm)/Cu (20 μm) (Fig. 1a top left) is utilized to fabricate the stretchable electrodes that interconnect a 4×5 array of transducers in the device (Detailed fabrication process appears in Methods). The transducers can be individually addressed by 20 stimulating electrodes on the top and a common ground at the bottom. The array design aims to map the vessels' positions, thus enabling sensing and monitoring using the exact transducer overlaying above the targeted vessel without tedious manual positioning (Supplementary note 6; Supplementary Fig. 11). The top simulating electrodes and the bottom ground are routed to the same plane by a vertical-interconnect-access (VIA) for optimized mechanical robustness and ease of electrical bonding (Fig. 1a, Supplementary Fig. 12, and Supplementary note 7).

The working principle is illustrated in Fig. 1a bottom. Technically, the device can continuously record the pulsating blood vessel diameter, which will be translated into localized BP waveforms[32]. Next, the BP waveform can be calculated as:

$$p(t) = p_d \cdot e^{\alpha\left(\frac{A(t)}{A_d} - 1\right)}$$

where p_d is the diastolic pressure, which will be acquired on the brachial artery using a BP cuff, and A_d is the diastolic arterial cross-section and α is the vessel rigidity coefficient. Assuming that artery is rotationally symmetrical, $A(t)$ can be calculated as:

$$A(t) = \frac{\pi d^2(t)}{4}$$

where $d(t)$ is the diameter waveform of the target artery. Detailed working principle, resolution, calibration, and validation of our device appear in Methods section, Supplementary notes 8 and 9. When the device is softly laminated on the skin (Supplementary Fig. 13), each transducer can be individually activated and controlled with a

power consumption of 23.6 mW. When the ultrasonic wave reaches interfaces, both transmission and reflection will occur. The transmission wave with reduced intensity allows penetrating into deeper layers of tissues. The reflection wave that carries critical location information of the interfaces (e.g., the anterior and posterior walls) can be sensed by the same transducer[33]. The vessel diameter measurement results are validated by clinical ultrasonography with excellent correspondence (99.7%, Supplementary Fig. 14). At a high pulse repetitive frequency (2000 Hz), the time of flight (TOF) signals corresponding to the pulsating anterior and posterior walls can be accurately recorded by an oscilloscope with 2 GHz sampling frequency, which will appear as separate and shifting peaks in the amplitude mode (Fig. 1a right bottom). The device can capture the pulsating blood vessel diameter dynamically with high spatial resolution (axial resolution 0.77 μm) and temporal resolution (500 μs).

The entire device is encapsulated by a silicone elastomer whose modulus is on par with that of the human skin. The elastomer is only 15 μm thick to balance a trade-off between mechanical robustness and sufficient acoustic emission performance (Supplementary Fig. 15, Supplementary note 5). Hydrophobic nature of the silicone elastomer provides a barrier for moisture, which protects the device from possible sweat corrosion (Fig. 1b). Due to its soft mechanics, the as-fabricated ultrasound patch allows conforming to both developable (Fig. 1b left) and non-developable surfaces (Fig. 1b middle). Also, the device is robust and can endure twisting and stretching (Fig. 1b right), showing its high potential for skin integration purposes.

Device characterization.

The piezoelectric transducer converts electrical potential between the top and bottom electrodes to mechanical vibrations, and vice versa. The efficiency of this process is exhibited by the measured impedance and phase angle spectra (Fig. 2a), showing excellent piezoelectricity whose k_{33} was measured to be 0.81, much higher than that of bulk PZT (~0.58)[33] due to its anisotropic high aspect ratio rod configuration compared with the isotropic bulk PZT[34]. The transducer performance is evaluated on the wrist ulnar artery of a healthy male. The echo signal appears in Fig. 2b, in which the TOF of the two peaks corresponds to the positions of the anterior and posterior walls of the ulnar artery, respectively. Signal analysis in the time and frequency domains of the posterior wall is illustrated in Fig. 2c, demonstrating that the material has a central frequency of 7.5 MHz and possesses good sensitivity of 32% at −6 dB bandwidth (Methods section) and a peak to peak voltage of 100 mV. Prediction of the beam pattern (Matlab R2016b, TAC_GUI toolbox) of our stretchable ultrasonic device appears in Fig. 2d. The results show that in the longitudinal direction, the conformal probe has excellent beam directivity and sufficient penetration for deep tissue detection, reaching a penetration depth of up to 40 mm (with the piezoelectric transducer size of 0.9*0.9 mm^2). The larger the piezoelectric material size, the deeper the ultrasonic wave can penetrate (Supplementary Fig. 16). The 1–3 composite has a low acoustic impedance (17 MRayl), which provides excellent acoustic coupling with the human skin. Additionally, the bottom circular electrode diameter is designed to be 0.6 mm to balance the practical bonding robustness and impedance matching (Supplementary Fig. 17).

The elastomeric matrix with iterative stretchable circuit designs and ultrathin encapsulation assemblies provides exceptionally conformal contacts to the human skin under various deformation modes (Supplementary Fig. 18). The device can be reversibly stretched up to 30% in the x-direction and 25% in the y-direction. The maximum stretchability can reach up to 60% in the x-direction and 50% in the y-direction (Fig. 2e). These mechanical characteristics enable robust and seamless contact with the skin (Supplementary note 10), given the fact that the human skin typically exhibits a linear elastic response to tensile strain <20%[35]. The electrical performance of the device remains stable under stretching and moist environment (Supplementary Fig. 19). Cell viability testing under controlled ultrasound intensity is shown in Fig. 2f and Supplementary Fig. 20. The fibroblast cells (HFF-1) are cultured under the ultrasonic wave emission from our conformal probe with a 100% survival rate after 16 hours of continuous exposure, showing excellent biocompatibility of our device (Detailed cell information appears in the Methods section).

Performance validation.

A conformal and intimate contact between the device and the human skin is paramount for the robust performance of the device. Continuous measurements on the radial artery using our device and a commercial tonometer, the noninvasive gold standard for BP waveform measurements, when the wrist is bent to different angles are shown in Fig. 3a. In this scenario, the tonometer needs to be held tightly by the operator to remain stable on the wrist, resulting in not only great pressure (~100 Pa) to skin, which causes severe irritation (Fig. 3b), but also significant waveform distortion and erroneous readings (Fig. 3c). However, our device self-adheres to the skin and adds minimal pressure (~5 Pa) to the skin due to its ultra-lightweight (0.15 g) and skin-like modulus. This unique feature enables the device to not only monitor in long-term without any discomfort but also maintain relatively stable and continuous recording even during motion. The correlation curves of these two devices are shown in Fig. 3d. Most importantly, our device has smaller relative measurement uncertainty (1%), higher measurement precision (within 2 mmHg), and higher accuracy (grade A) than the commercial equipment (Supplementary note 11, Methods section, and Supplementary Figs. 21 and 22). Furthermore, the tonometer is highly operator-dependent, which is reflected by the fact that either tiny offset from the central arterial axis or moderate holding forces of the tonometer probe will introduce tremendous recording error of the BP waveform (Supplementary Figs. 23 and 24). Our conformal ultrasonic array with the ultra-lightweight and vessel positioning capability demonstrated above exhibits substantial advantages over the applanation tonometry.

More interestingly, the conformal ultrasound probe enables a gel-free working mode. Traditional ultrasonic transducer highly relies on ultrasound gel to eliminate interfacial air gaps between the probe and the skin for good acoustic coupling. The gel is unpleasantly cold and has to be frequently reapplied to prevent it from drying out. In this device, we add a 15 μm thick layer of silicone as the acoustic coupling layer. The silicone is sticky and ultra-low modulus (~5 kPa) to ensure intimate contact with the skin without applying any gel. The quality of the acquired signals and waveforms is comparable to those acquired with the gel (Supplementary Fig. 25 and Methods section). Moisture/human sweat that significantly influences the PPG measurements does not affect the performance of the conformal

ultrasound device (Supplementary Fig. 26). The excellent design enables the device with remarkable durability, allowing highly reproducible testing results after four weeks (Supplementary Fig. 27).

Dynamic hemodynamics monitoring.

Due to its excellent mechanical compliance and lightweight, our device can maintain intimate and stable contact with the human skin both mechanically and acoustically in different body postures with pure van der Waals force (Supplementary Fig. 28). During exercise, the muscles require more delivery of nutrients and oxygen, so the cardiac output increases to meet the need[36]. On the one hand, human vessels dilate to increase the delivery, so the vascular resistance and reflection are reduced. On the other hand, the heart rate and systolic strength increase to boost up the cardiac output. The measured heart rates on radial artery during resting (~75/min) and immediately after exercise (~112/min) are shown in Fig. 3e. The BP waveform has a higher systolic peak due to the stronger ventricular systole to get more substantial cardiac output[37]. The averaged waveform morphology changes before and after intense exercise appear in Fig. 3f (normalized to same systolic and diastolic pressure values), showing a steep drop of the systolic peak after physical training due to the vasodilation induced vascular resistance decrease. It is worth noting that we need to calibrate our device before and after exercise that will significantly change the diastolic pressure. However, we can observe the vessel dilation and vascular resistance decrease by comparing the normalized waveforms, regardless of what the absolute BP values are.

CBP recording.

From the pathophysiological perspective, the CBP waveform is a crucial and the most direct predictor of main cardiovascular events[5]. Monitoring those events in a continuous and long-term manner can lead to remarkable advancements in cardiovascular disease diagnosis and prevention[6], which are yet to be realized by existing medical tools (Supplementary note 12). We demonstrate highly accurate direct measurements of the central vasculatures pulsating behavior in deep tissues, including the carotid artery and internal and external jugular veins. Schematic illustration of the measurement configuration appears in Fig. 3g. The carotid artery (CA, ~25 mm underneath the skin with slight individual variations[38], near the central aorta) carries a significant amount of blood from the left ventricle (LV) and left atrium (LA) to the rest of the body. A typical period of the carotid artery BP waveform measured by our device shows a clear systolic peak and dicrotic notch (Fig. 3h). The former indicates the ventricular systole and the latter suggests the closure of the aortic valve. The detailed CBP measurement calibration appears in Supplementary note 9. The corresponding validation using the commercial tonometer exhibits remarkable correspondence (Supplementary Fig. 29). The blood flow sequence in the central cardiovascular system and direct relationship between the central vessels and the heart appears in Supplementary Fig. 30. Detailed clinical meaning of arterial BP waveforms is illustrated in Supplementary Fig. 31 and discussed in Supplementary note 13.

The internal jugular vein, carrying the venous blood to the right atrium and right ventricle and finally to the lung, reflects the right heart activities. A typical jugular venous pressure waveform measured by our device appears in Fig. 3i. The normalized pressure waveform is

obtained by the volume assessment method[39]. Associated algorithms and equations of this method are discussed in details in Supplementary note 9. The jugular venous waveform comprises three characteristic peaks: A (Atrial contraction), C (Tricuspid bulging, ventricular contraction), and V (Systolic filling of the atrium); and two descents: X (Atrial relaxation) and Y (Early ventricular filling). Those components correspond to various events during each cardiac cycle. The jugular venous waveform measured by clinical color Doppler imaging machine on the same subject appears in Supplementary Fig. 32, showing the corresponding A, C, and X peaks and V and Y descents. The jugular venous distension (JVD), seen as a vessel bulging on the neck created by deep exhalation of the subject (Supplementary Fig. 33), can predict right-side heart failure[40]. More detailed discussions are included in Supplementary note 13.

BP waveform monitoring from central to peripheral.

Due to the amplification effect, namely the progressive vascular resistance, stiffness, and impedance mismatch between central and peripheral vessels, the arterial pressure waveform varies from central to peripheral[6]. Although the diastolic and mean arterial pressures are relatively constant, systolic pressure can be up to 40 mmHg higher in the peripheral than the central artery[41]. This amplification effect on the various part of the body contains abundant information related to age, gender, height, heart rate, and systematic diseases affecting the vasculature[42]. Those data, if carefully collected, can be critical for improving the efficacy of diagnosis and prognosis of cardiovascular diseases[43]. However, in current clinical settings, those valuable data and signals can only be obtained by the professional clinician in a considerably infrequent manner. The challenges for existing approaches are discussed in Supplementary note 12.

Our device allows observing this intriguing phenomenon. The amplification effect will increase as we move from the large and highly elastic central arteries (e.g., the carotid) to the small and stiff peripheral artery (e.g., the radial and dorsalis pedis) (Fig. 4, the first row and Supplementary Fig. 34). This phenomenon is due to the backward propagation of pulse waves generated at the arterioles. At the central cite, those reflected pulses need to travel a long distance so they adds to the CBP waveform in a misaligned manner. On the contrary, at the peripheral site, they travel a much shorter distance so they instantly contribute to the peripheral BP waveform in a way that is time-aligned. Therefore, the more peripheral the artery is, the higher the amplification/augmentation will be (Fig. 4, the second row). To validate this amplification effect, we use a commercial tonometer to test on the same subject. Remarkable corresponding results appear in the third row of Fig. 4. An exciting feature brought by this direct diameter measurement approach is that it allows observing this amplification phenomenon and deriving accurate pulse pressure values from multiple body parts simultaneously by the diastolic pressure at only the brachial site, with no site mismatch (Supplementary note 14 and Supplementary Fig. 35). The upstroke gradient increases as a result of the pressure amplification (Supplementary Fig. 36 and Supplementary note 15).

Another notable feature of the BP waveforms is the progressive time interval between the systolic peak and the dicrotic notch, which is illustrated by the grey area. When the pressure wave travels down from the central arteries, its magnitude increases due to impedance

mismatches encountered on the way, which creates a reflected wave that travels back to the heart during late systole and early diastole. This reflection wave takes a longer time to travel from a location that is more distant from the heart, and thus contributes to an increase in the time interval between the systolic peak and the dicrotic notch (gray areas in the waveforms in Fig. 4, the third row)[44]. The capability of capturing those systemic variations demonstrates the device's potential for accurate clinically relevant diagnosis.

Electrocardiogram (ECG) correlation for arterial stiffness calculation.

Characteristics of the arterial pulse propagation possess a strong relationship with vascular stiffness, which is one of the key determinants of cardiovascular risks[45]. Among all vascular parameters, pulse wave velocity (PWV), is the most accessible and reliable way to evaluate the arterial stiffness (Supplementary note 16) and can be calculated as follows[46]:

$$PWV = \frac{D}{PAT}$$

where D is the distance between the ECG sensor and the ultrasonic sensor. The measurement schematics are shown in Fig. 5a, with the simultaneous measurements of ECG and pulse arrival times (PATs) at three different sites including brachial, radial, and dorsalis pedis. Figures 5b-d present the ECG correlation results: Case 1, brachial artery (Fig. 5b); Case 2, radial artery (Fig. 5c); and Case 3, pedal artery (Fig. 5d), where ECG is measured on the chest for all three cases (Supplementary Fig. 37). As seen in Figs. 5b-d, PWV in Case I is 5.4 m/s, where D is 54 cm and time difference is 100 ms; PWV in Case II is 5.8 m/s, where D is 104 cm and time difference is 180 ms; PWV in Case III is 5.3 m/s, where the D is 159 cm and the time difference is 300 ms. The PWV measurements are highly reproducible (Supplementary Fig. 38) and have been validated by the commercial equipment, shown in Fig. 5e and Supplementary Fig. 39 (Detailed testing condition and measurement methods appears in the Methods section).

Discussion

He have shown a new class of conformal and stretchable ultrasonic devices that offer noninvasive, accurate, and continuous monitoring of vital signs from well below the human skin, adding a new dimension to the sensing range of conventional stretchable electronics. This device exploits strategic material integration and advanced microfabrication techniques to achieve both state-of-the-art functions and suitable mechanical compliance that allows intimate coupling with the human skin. This device can be used to capture a series of key features in the central blood vessels with reliable performance, holding strong clinical implications.

Device performance and functionality could be improved. The measurement of absolute pressure using PAT is feasible by ECG correlation, bypassing the need for re-calibration with the BP cuff (Supplementary note 16). Furthermore, ultrasonic imaging on the human body could provide the accurate cross-sectional area of the vessel for calculating the BP waveform, which is especially valuable for the CVP measurement on the irregularly shaped jugular vein. Additionally, integrating the post-end functions such as the electronic control,

signal processing, waveform pattern recognition, wireless communications, and power sources in a stretchable and lightweight format would significantly enhance device wearability. To reduce the system-level power consumption, a lower sampling rate analog-to-digital converter could be used to decrease the power budget of data transmission. And a phased-array control algorithm could be implemented to allow the focusing and steering of the ultrasonic beam inside the human body.

Methods

1. Fabrication of the stretchable ultrasonic device.

The fabrication can be summarized into three parts: (1) stretchable circuit patterning; (2) transfer printing; and (3) soft elastomeric packaging (Supplementary Fig. 40). First, a Cu foil (20 μm thick, MicroThin, Oak-Mitsui Inc.) was coated with PI from poly(pyromellitic dianhydride-co-4, 40-oxydianiline) amic acid solution. This process was performed at 4000 rpm for 60 s. And then the foil was soft baked on a hotplate at 110 °C for three minutes and 150 °C for one min, and then cured in a nitrogen oven at 300 °C for 1 h. A glass slide coated with a layer of polydimethylsiloxane (PDMS, Sylgard 184® silicone elastomer, 20:1) served as the substrate to laminate the Cu foil with the PI layer in contact with the PDMS. UV ozone surface activation for 3 min was used to increased the bonding between the PI and PDMS. Then, a laser ablation system (Supplementary Fig. 41), 0.342 mJ power, 900 kHz pulse repetition frequency, 300 mm/s laser cutting speed, and 241 ns pulse width, was utilized to create the circuit pattern with the highest resolution (Supplementary Fig. 42). After that, using water-soluble tape (Aquasol), the circuit was transferred on a 15 μm thick Eco-flex (0030®, Smooth-On) substrate spin-coated on a glass slide (Supplementary Fig. 43). After removing the water soluble tape, the circuit surface was cleaned using flux to remove the surface oxidation (Supplementary Fig. 44) created during the laser ablation process to increase the welding strength. The welding with the top and bottom electrodes was achieved with the solder paste at 150 °C for 5 min. After that, the device was encapsulated with Eco-flex. Curing was done at room temperature for 2 hours, and then the glass slides were peeled off. Finally, spin-coating an additional layer of silbione on the Ecoflex substrate facilitates removing the interfacial gap and thus the necessity of the gel during testing.

2. Poling of the 1–3 composite.

Poling the 1–3 composite (Smart Material Corp.) increased its piezoelectric coefficient and electromechanical coupling factor of the composite[47]. The poling involved using an electric field to align the dipoles of the piezoelectric materials, which enhances the piezoelectricity and performance of the device[48]. The polarizing hysteresis loop (Supplementary Fig. 45) was measured in silicone oil. The poling of the device was implemented at d.c. 1.2 kV/cm for 15 min. An excessive poling electric field caused breakdown of the piezoelectric materials, thus reducing the signal strength (Supplementary Fig. 46).

3. Measurement and data analysis of the BP waveforms.

The BP waveform measurement was carried out on a healthy male of age 22, under the approval by the Institutional Review Board of the University of California, San Diego (IRB

no. 170812). Written informed consent was obtained from all the human subjects. All measurements were carried out on the subject when sitting. The measurement setup is illustrated in Supplementary Fig. 47. A layer of Silbione® was applied at the bottom of the device surface to enable gel-free measurements. The signal analysis was based on the TOF analysis, which was the gauge of the time interval between the signal peak and zero-point time. The TOF was used to calculate the propagation distance, by multiplying the speed of ultrasound in the specimen. The device was activated by an ultrasonic pulser (Olympus 5077 PR) at 100 V, using the transmit/receive mode. The pulse repetitive frequency was 2000 Hz. The echo signal was received by a Picoscope (Picoscope 6404) with a temporal resolution of 500 μs, which allowed precise vessel wall tracking (Supplementary note 8). Discussions of measurement principle, resolutions, uncertainty, accuracy, and precision are illustrated in Supplementary notes 8 and 11 and Supplementary Figs. 22, and 48–50. The circuit enabling simultaneous measurement of pulse pressure in varies site is illustrated in Supplementary note 14 and Supplementary Fig. 51. The clinical color Doppler machine (Mindray DC 7) was used to confirm the characteristic peaks in the venous waveform. The BP waveform measurement results were validated by a SphygmoCor EM3® tonometer.

4. ECG correlation.

The ECG correlation to the BP waveforms at different locations was taken on the same subject, when sitting, consecutively with a two-minute interval, to guarantee the subject had a relatively constant BP value and arterial stiffness. The longest duration of skin integration on the same skin region was two hours. No allergic reactions, redness, or damage to the skin were observed in any of our studies. The diastolic pressure was calibrated using a commercial BP cuff (Smart Logic Technology, 6016) before each monitoring period. Additionally, the testing subject maintained a stable physiological and psychological status to guarantee stable levels of BP and vasculature stiffness. A detailed discussion of PAT, pulse transit time (PTT), and PWV is illustrated in Supplementary Fig. 52 and Supplementary note 16.

5. Transducer selection, bandwidth, and resolution characterization.

In the experiments, we chose piezoelectric ultrasound transducers (PUTs) instead of capacitive micromachined ultrasound transducers (cMUTs) or piezoelectric micromachined ultrasound transducers (pMUTs), because of the low cost and ease of fabrication of PUTs. More detailed considerations are presented in Supplementary note 5 and Supplementary Fig. 53. The transducer bandwidth (32%) was calculated by using the frequency range (2.4 MHz) divided by central frequency (7.5 MHz). The axial resolution characterization exploited a thin metal wire suspended at the center of a beaker filled with water. A 1×10 linear array of transducers was fabricated and attached to the beaker wall parallel to the ground. All signals of the ten transducer elements were acquired and combined with one transducer as the transmitter and the other as the receiver (e.g., 1T2R, 1T3R…1T10R; 2T1R, 2T3R…2T10R; …; 10T1R, 10T2R….10T9R). The total 90 signals were used, by the delay-and-sum (DAS) reconstruction algorithm, to reconstruct the image (Supplementary Fig. 10c). The obtained image with low-level side lobes resulted from the reconstruction algorithm and the limited number of elements used for imaging.

6. Cell viability assay under ultrasound exposure.

The human skin fibroblast cells (HFF-1) were first purchased from American Type Culture Collection (ATCC) and cultured in Dulbecco's Modified Eagle's Medium (DMEM, Gibco) supplemented with 10% fetal bovine serum (FBS, Gibco) and 1% penicillin/streptomycin (Gibco) under 37 °C within 5% CO_2. Then the HFF-1 cells were subcultured and seeded into 24-well plate at the density of 1×10^4/ml and incubated for another 24 hours. No antibodies were used in the experiment. Then a beam of ultrasound at the frequency of 7.5 MHz was applied to the bottom of the culture plate. After 2, 6, and 16 hours' ultrasound exposure, the cells were stained with calcein AM (Invitrogen, 3M, excitation/emission = 488 nm/525 nm) and propidium iodide (PI, Invitrogen, 3M, excitation/emission = 530 nm/620 nm) for 15 min, and then were imaged under fluorescence microscopy (EVOS, Thermofisher Scientifics). For the positive control group, the cells were treated with 75% ethanol for 10 min.

Supplementary Material

Refer to Web version on PubMed Central for supplementary material.

Acknowledgments

References

1. McGhee BH & Bridges EJ Monitoring arterial blood pressure: what you may not know. Crit. Care Nurse 22, 60–79 (2002).

2. Avolio AP, Butlin M & Walsh A Arterial blood pressure measurement and pulse wave analysis—their role in enhancing cardiovascular assessment. Physiol. Meas 31, 275–290 (2009).

3. Kumar A et al. Pulmonary artery occlusion pressure and central venous pressure fail to predict ventricular filling volume, cardiac performance, or the response to volume infusion in normal subjects. Crit. Care Med 32, 691–699 (2004). [PubMed: 15090949]

4. Dagdeviren C et al. Conformable amplified lead zirconate titanate sensors with enhanced piezoelectric response for cutaneous pressure monitoring. Nat. Commun 5, 4496–4506 (2014). [PubMed: 25092496]

5. Safar ME et al. Central pulse pressure and mortality in end-stage renal disease. Hypertens 39, 735–738 (2002).

6. Trudeau L Central blood pressure as an index of antihypertensive control: determinants and potential value. Can. J. of Cardiol 30, 23–28 (2014).

7. McEniery CM, Cockcroft JR, Roman MJ, Franklin SS & Wilkinson IB Central blood pressure: current evidence and clinical importance. Eur. Heart J 35, 1719–1725 (2014). [PubMed: 24459197]

8. Ding F-H et al. Validation of the noninvasive assessment of central blood pressure by the SphygmoCor and Omron devices against the invasive catheter measurement. Am. J. of Hypertens 24, 1306–1311 (2011). [PubMed: 21976274]

9. Agabiti-Rosei E et al. Central blood pressure measurements and antihypertensive therapy. Hypertens 50, 154–160 (2007).

10. Bruyndonckx L et al. Methodological considerations and practical recommendations for the application of peripheral arterial tonometry in children and adolescents. Int. J. Cardiol 168, 3183–3190 (2013). [PubMed: 23972967]

11. Avolio AP et al. Role of pulse pressure amplification in arterial hypertension. Hypertens 54, 375–383 (2009).

12. Williams B et al. Differential Impact of Blood Pressure–Lowering Drugs on Central Aortic Pressure and Clinical Outcomes. Circulation 113, 1213–1225 (2006). [PubMed: 16476843]

13. Moffitt EA et al. Rate-pressure product correlates poorly with myocardial oxygen consumption during anaesthesia in coronary patients. Can. J. Anaesth 31, 5–12 (1984).

14. Roman MJ et al. Relations of central and brachial blood pressure to left ventricular hypertrophy and geometry: the Strong Heart Study. J. Hypertens 28, 384–388 (2010). [PubMed: 20051906]

15. Chen C-H et al. Different effects of fosinopril and atenolol on wave reflections in hypertensive patients. Hypertens 25, 1034–1041 (1995).

16. Pini R et al. Central but not brachial blood pressure predicts cardiovascular events in an unselected geriatric population: the ICARe Dicomano Study. J. Am. Coll. Cardiol 51, 2432–2439 (2008). [PubMed: 18565402]

17. Langewouters G, Settels J, Roelandt R & Wesseling K Why use Finapres or Portapres rather than intraarterial or intermittent non-invasive techniques of blood pressure measurement? J. Med. Eng. Technol 22, 37–43 (1998). [PubMed: 9491357]

18. Kim J et al. Battery-free, stretchable optoelectronic systems for wireless optical characterization of the skin. Sci. Adv 2, 1–10 (2016).

19. Schwartz G et al. Flexible polymer transistors with high pressure sensitivity for application in electronic skin and health monitoring. Nat. Commun 4, 1859–1870 (2013). [PubMed: 23673644]

20. Sandberg M, Zhang Q, Styf J, Gerdle B & Lindberg LG Non-invasive monitoring of muscle blood perfusion by photoplethysmography: evaluation of a new application. Acta Physiol 183, 335–343 (2005).

21. Hertzman AB The blood supply of various skin areas as estimated by the photoelectric plethysmograph. Am. J. Physiol. Cell Physiol 124, 328–340 (1938).

22. Maeda Y, Sekine M & Tamura T Relationship between measurement site and motion artifacts in wearable reflected photoplethysmography. J. Med. Syst 35, 969–976 (2011). [PubMed: 20703691]

23. Xing X & Sun M Optical blood pressure estimation with photoplethysmography and FFT-based neural networks. Biomed. Opt. Express 7, 3007–3020 (2016). [PubMed: 27570693]

24. Drzewiecki GM, Melbin J & Noordergraaf A Arterial tonometry: review and analysis. J. Biomech 16, 141–152 (1983). [PubMed: 6863329]

25. Howard G et al. Carotid artery intimal-medial thickness distribution in general populations as evaluated by B-mode ultrasound. Stroke 24, 1297–1304 (1993). [PubMed: 8362421]

26. Rotenberg MY & Tian B Bioelectronic devices: Long-lived recordings. Nat. Biomed. Eng 1, 48–50 (2017).

27. Kim D-H et al. Epidermal electronics. Science 333, 838–843 (2011). [PubMed: 21836009]

28. Yokota T et al. Ultraflexible, large-area, physiological temperature sensors for multipoint measurements. Proc. Natl. Acad. Sci 112, 14533–14538 (2015). [PubMed: 26554008]

29. Gao W et al. Fully integrated wearable sensor arrays for multiplexed in situ perspiration analysis. Nature 529, 509–514 (2016). [PubMed: 26819044]

30. Martín A et al. Epidermal Microfluidic Electrochemical Detection System: Enhanced Sweat Sampling and Metabolite Detection. ACS Sens 2, 1860–1868 (2017). [PubMed: 29152973]

31. Huang X et al. Materials and designs for wireless epidermal sensors of hydration and strain. Adv. Funct. Mater 24, 3846–3854 (2014).

32. Arndt JO, Klauske J & Mersch F The diameter of the intact carotid artery in man and its change with pulse pressure. Pflugers. Arch 301, 230–240 (1968).

33. Zhou Q, Lam KH, Zheng H, Qiu W & Shung KK Piezoelectric single crystal ultrasonic transducers for biomedical applications. Prog. Mater. Sci 66, 87–111 (2014). [PubMed: 25386032]

34. Sun P et al. High frequency PMN-PT 1–3 composite transducer for ultrasonic imaging application. Ferroelectrics 408, 120–128 (2010). [PubMed: 21869845]

35. Arumugam V, Naresh M & Sanjeevi R Effect of strain rate on the fracture behaviour of skin. J. Biosci 19, 307–313 (1994).

36. Kitamura K, Jorgensen CR, Gobel FL, Taylor HL & Wang Y Hemodynamic correlates of myocardial oxygen consumption during upright exercise. J. Appl. Physiol 32, 516–522 (1972). [PubMed: 5026501]

37. Ishibashi Y, Duncker DJ, Zhang J & Bache RJ ATP-sensitive K+ channels, adenosine, and nitric oxide–mediated mechanisms account for coronary vasodilation during exercise. Circ. Res 82, 346–359 (1998). [PubMed: 9486663]

38. Wain RA et al. Accuracy of duplex ultrasound in evaluating carotid artery anatomy before endarterectomy. J. Vasc. Surg 27, 235–244 (1998). [PubMed: 9510278]

39. Donahue SP, Wood JP, Patel BM & Quinn JV Correlation of sonographic measurements of the internal jugular vein with central venous pressure. Am. J. Emerg. Med 27, 851–855 (2009). [PubMed: 19683116]

40. Butman SM, Ewy GA, Standen JR, Kern KB & Hahn E Bedside cardiovascular examination in patients with severe chronic heart failure: importance of rest or inducible jugular venous distension. J. Am. Coll. Cardiol 22, 968–974 (1993). [PubMed: 8409071]

41. Mukkamala R & Xu D Continuous and less invasive central hemodynamic monitoring by blood pressure waveform analysis. Am. J. Physiol. Heart Circ. Physiol 299, 584–599 (2010).

42. Camacho F, Avolio A & Lovell N Estimation of pressure pulse amplification between aorta and brachial artery using stepwise multiple regression models. Physiol. Meas 25, 879–889 (2004). [PubMed: 15382828]

43. Williams B et al. Differential impact of blood pressure–lowering drugs on central aortic pressure and clinical outcomes: principal results of the Conduit Artery Function Evaluation (CAFE) study. Circulation 113, 1213–1225 (2006). [PubMed: 16476843]

44. Shirwany NA & Zou M.-h. Arterial stiffness: a brief review. Acta Pharmacol. Sin 31, 1267–1276 (2010). [PubMed: 20802505]

45. DeLoach SS & Townsend RR Vascular stiffness: its measurement and significance for epidemiologic and outcome studies. Clin. J. Am. Soc. of Nephrol 3, 184–192 (2008). [PubMed: 18178784]

46. Mukkamala R et al. Toward ubiquitous blood pressure monitoring via pulse transit time: theory and practice. IEEE Trans. Biomed. Eng 62, 1879–1901 (2015). [PubMed: 26057530]

47. Ren K, Liu Y, Geng X, Hofmann HF & Zhang QM Single crystal PMN-PT/epoxy 1–3 composite for energy-harvesting application. IEEE Trans. Ultrason. Ferroelectr. Freq. control 53, 631–638 (2006). [PubMed: 16555772]

48. Hu H et al. Stretchable ultrasonic transducer arrays for three-dimensional imaging on complex surfaces. Sci. Adv 4, eaar3979 (2018).
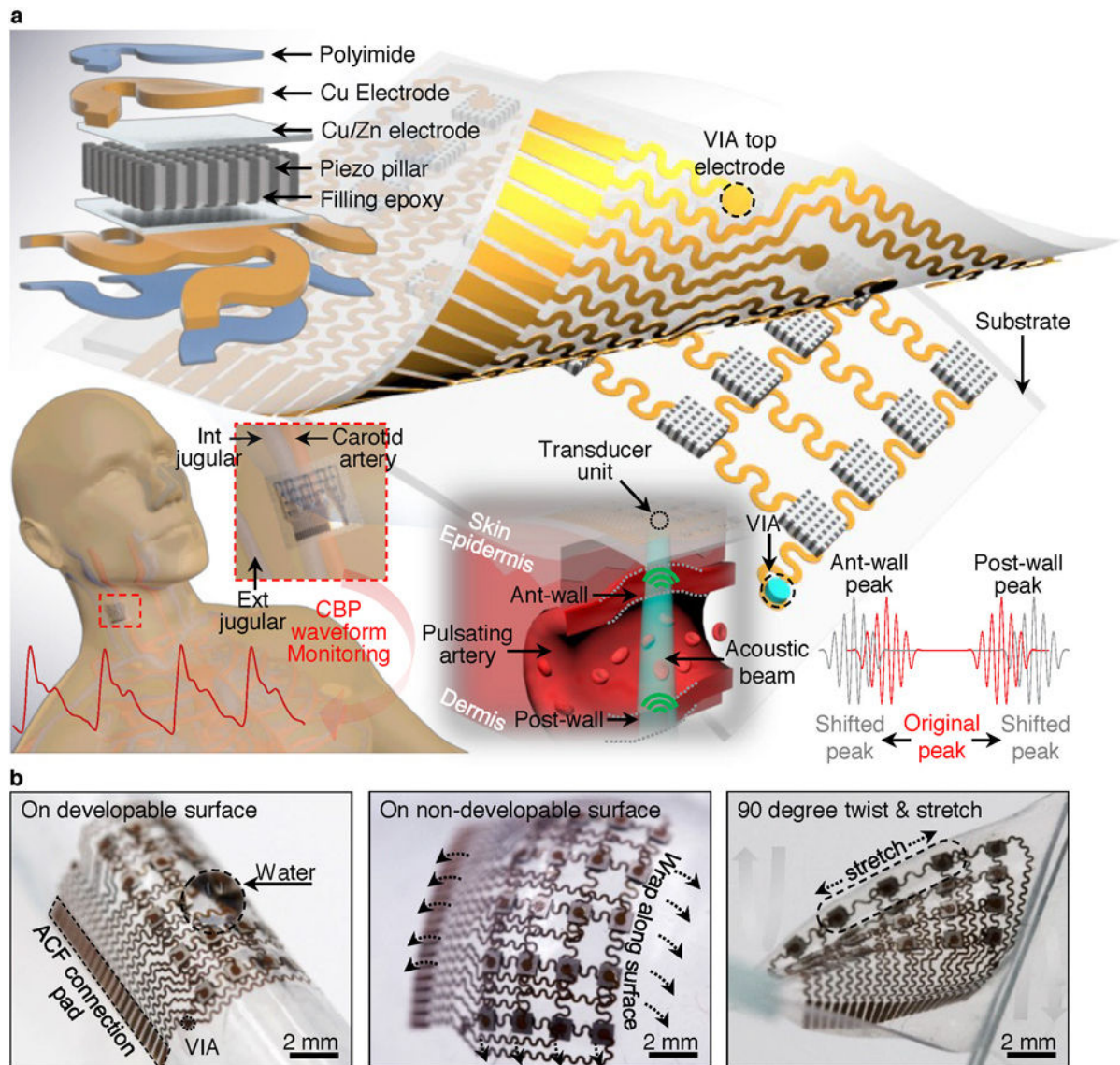
Figure | 1.

Design and working principle of the stretchable ultrasonic device. **a,** Schematics of the stretchable ultrasonic device, where key components are labeled. The high-performance 1–3 composite with periodic piezoelectric rods embedded in an epoxy matrix suppresses shear vibration modes and enhances longitudinal ultrasonic penetration into the skin. The vertical interconnect access (VIA) is used connect the top and bottom electrodes, allowing the co-planar anisotropic conductive film (ACF) bonding to the electrodes to enhance the robustness of the device. When mounted on the human neck, the device enables monitoring of CBP by capturing the pulsating vessel diameter of carotid artery, internal jugular vein (int jugular), and external jugular vein (ext jugular) using the pulse-echo method, as illustrated as the bottom left graph. The device can locate the dynamic anterior (ant) and posterior (post) walls of the vessel using high-directivity ultrasonic beam, as bottom middle graph shows. The corresponding shifting echo radio frequency signals reflected from the anterior and

posterior walls appear in the bottom right. **b**, The device conforming to complex surfaces and under mixed modes of stretching and twisting, demonstrating the mechanical compliance and robustness of the device. The large contact angle of the water droplet on the device in the left panel shows the hydrophobic properties of silicone encapsulation materials that can be used as a barrier to moisture/sweat.
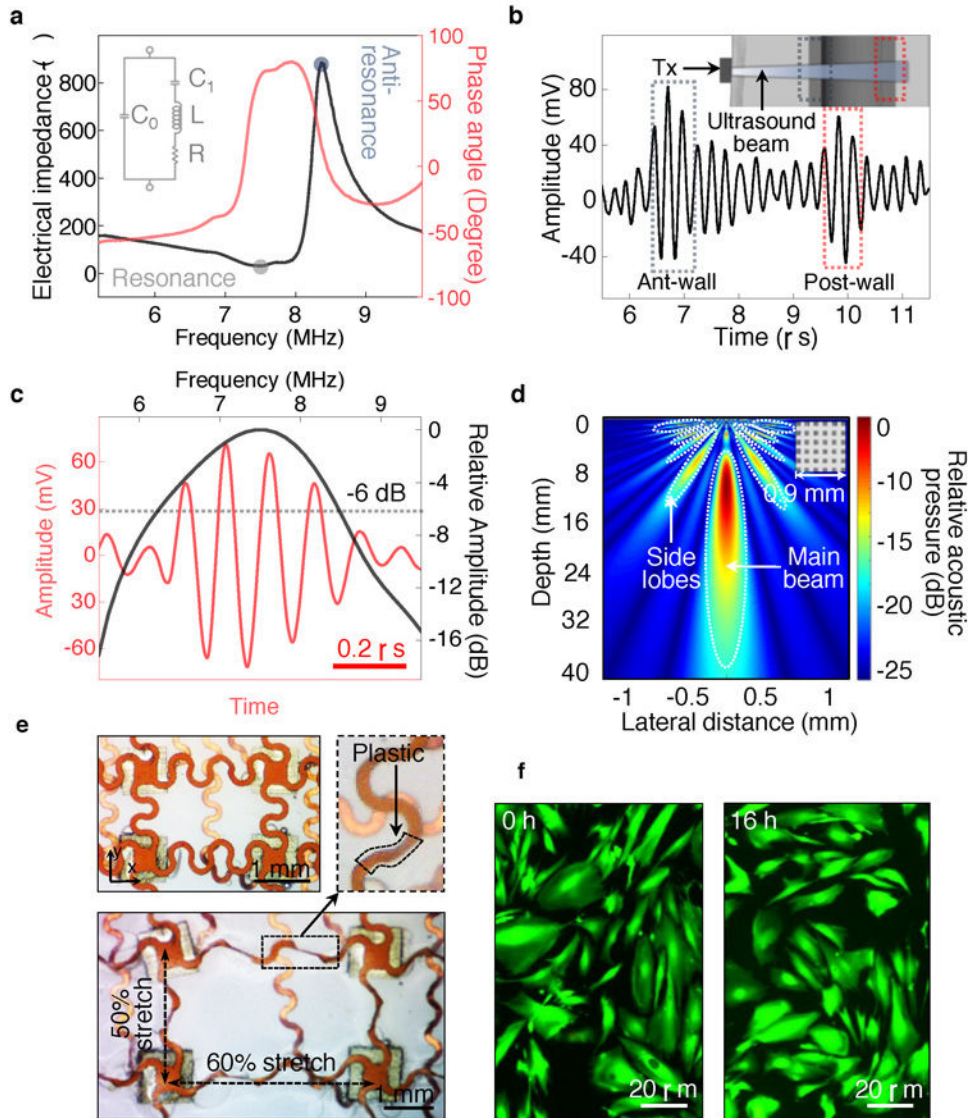
Figure | 2.

Electrical, mechanical, acoustical, and biocompatibility characterizations of the conformal ultrasonic device. **a,** Impedance and phase angle spectra of the 1–3 composite, showing the excellent piezoelectricity. The resonant and anti-resonant frequency ranges are labeled in shaded circles. The left inset is the equivalent RLC circuit diagram of the piezoelectric transducer. At the resonant frequency, the impedance of the equivalent circuit is at the minimum, which will be the most power efficient. At the anti-resonant frequency, the impedance of the equivalent circuit is at the maximum, and the transducer will have the largest damping. **b,** Ultrasonic receiving signals on the ulnar artery, with two clear echo peaks from the anterior (ant) and posterior (post) vessel walls. Inset is a schematic diagram representing the transducer and the ulnar artery to show echo peaks aligned with the ant and post vessel walls. Tx represents the transducer. **c,** Time and frequency domain characterization of the signal in **b** (post-wall peak), showing excellent signal quality and bandwidth (dashed line), indicating the high sensitivity of the transducer. **d,** Simulated

acoustic emission profile of a piezoelectric material size of 0.9×0.9 mm^2 (inset) with excellent beam directivity and penetration depth (>4 cm). **e,** Bi-axial tensile test of the device with stretchability up to 60% in the x-direction and 50% in y-direction without fracture. The zoomed-in image of the dashed box shows the slight plastic deformation when biaxial strain is larger than 30% in the x-direction. **f,** Fluorescent images of the fibroblast cells before (left panel) and after 16 hours (right panel) continuous exposure to the ultrasound generated by the conformal ultrasonic device. The 100% survival rate of the cells prove the excellent bio-compatibility of the conformal ultrasonic device.
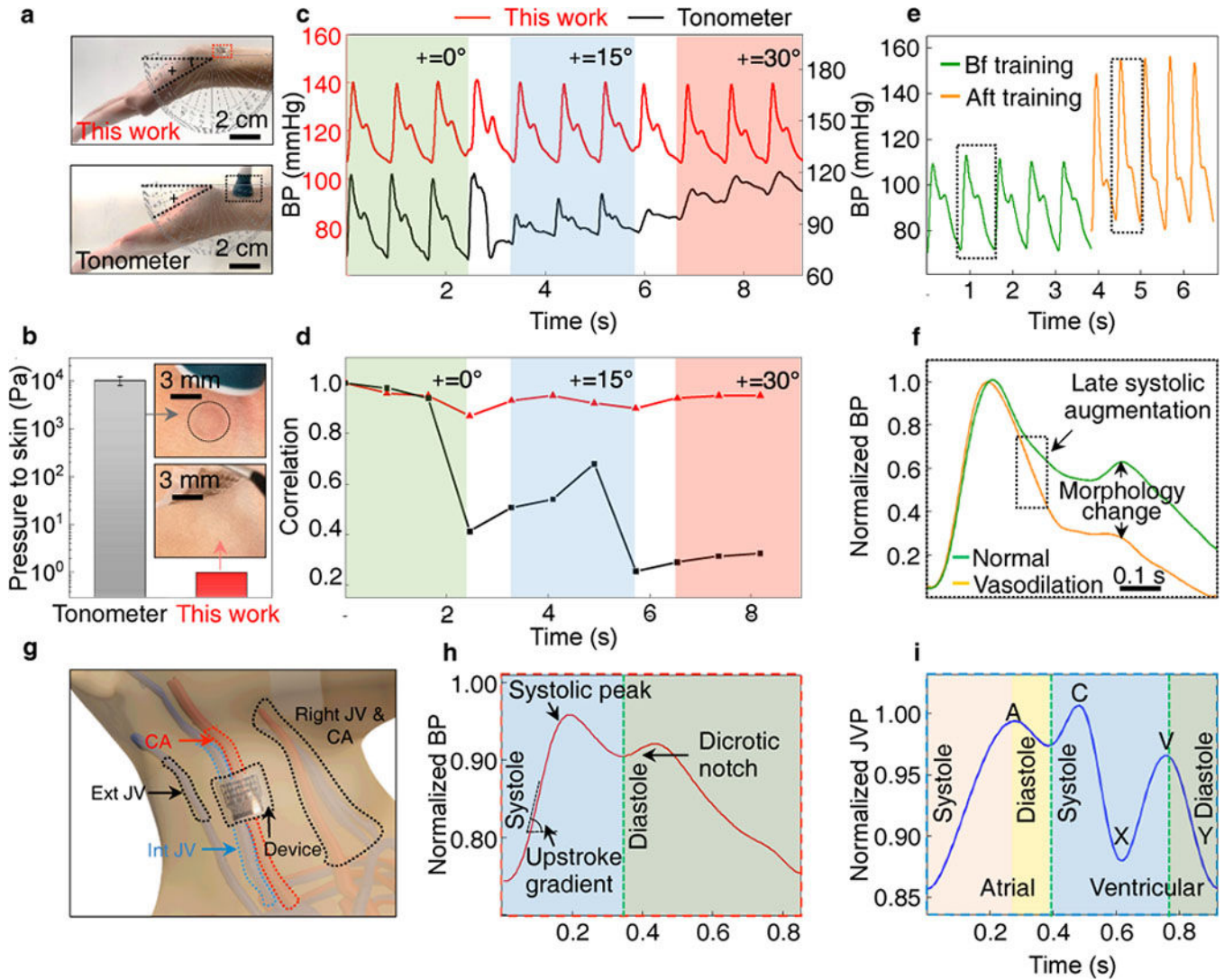
Figure | 3.

Comparison between the conformal ultrasound (US) sensor and the commercial tonometer, exercise hemodynamics monitoring, and central arterial and venous pulse measurements. **a,** Continuous measurements of radial pulse waveforms by both US sensor (top) and the commercial tonometer (bottom) under the same condition. **b,** Comparison of applied pressure levels to the skin during the measurement. Inset figures show the skin irritation brought by the tonometer and the conformal US sensor. Dots represent all data points. Error bars represent ± s.d. (N=4). **c,** Comparison of the BP waveforms measured continuously when wrist is bent at a rate of ~15°/s, showing the robust performance of the conformal device. Different postures from 0° to 30° are labeled in different shades. **d,** Autocorrelation of the waveforms in **c**, showing the conformal US device can maintain stable measurements in motion. **e,** Pulse waveforms on the radial artery before (bf) and after (aft) exercise, showing the changes in absolute pressure values and waveform morphologies. **f,** Pulse waveforms averaged from 10 continuous periods and normalized to the same diastolic and systolic pressure values to demonstrate the change in morphologies caused by vasodilation.

g, Illustration of the US sensor measurement locations marked with arrows: the left carotid artery (CA), external jugular vein (Ext JV) and internal jugular vein (Int JV). The right jugular vein and carotid artery are also highlighted. **h,** A typical pulse waveform measured from the carotid artery, directly correlated to the left atrial and ventricular events. Different phases and characteristic morphologies are marked. **i,** A typical pulse waveform from the internal jugular vein, directly correlated to right atrial and ventricular activities. Different phases and characteristic morphologies are marked.
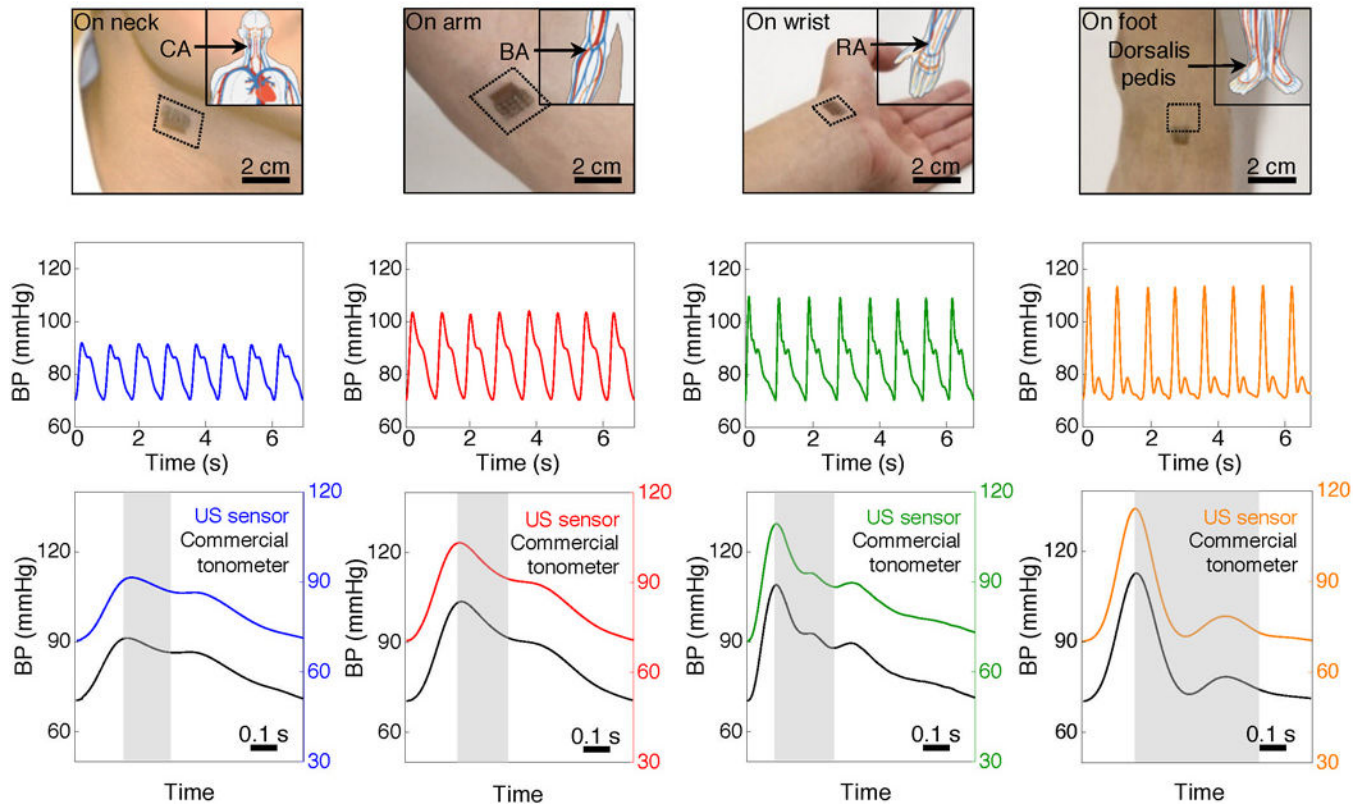
Figure | 4.

BP measurements from the central to peripheral arteries and validation using the commercial tonometer. Measurement positions (top row), collected arterial pressure waveforms (middle row), and the BP waveform of one period compared with results from the tonometer (bottom row). From the 1st column to 4th column are carotid artery (CA), brachial artery (BA), radial artery (RA), and pedal artery (Dorsalis pedis), respectively, showing an increase of the amplification effect by progressive vascular resistance, a longer interval time between systolic peak and dicrotic notch (illustrated by the grey area), a higher systolic pressure value, and a higher upstroke gradient (the slope of the BP waveform at the beginning of the upstroke).
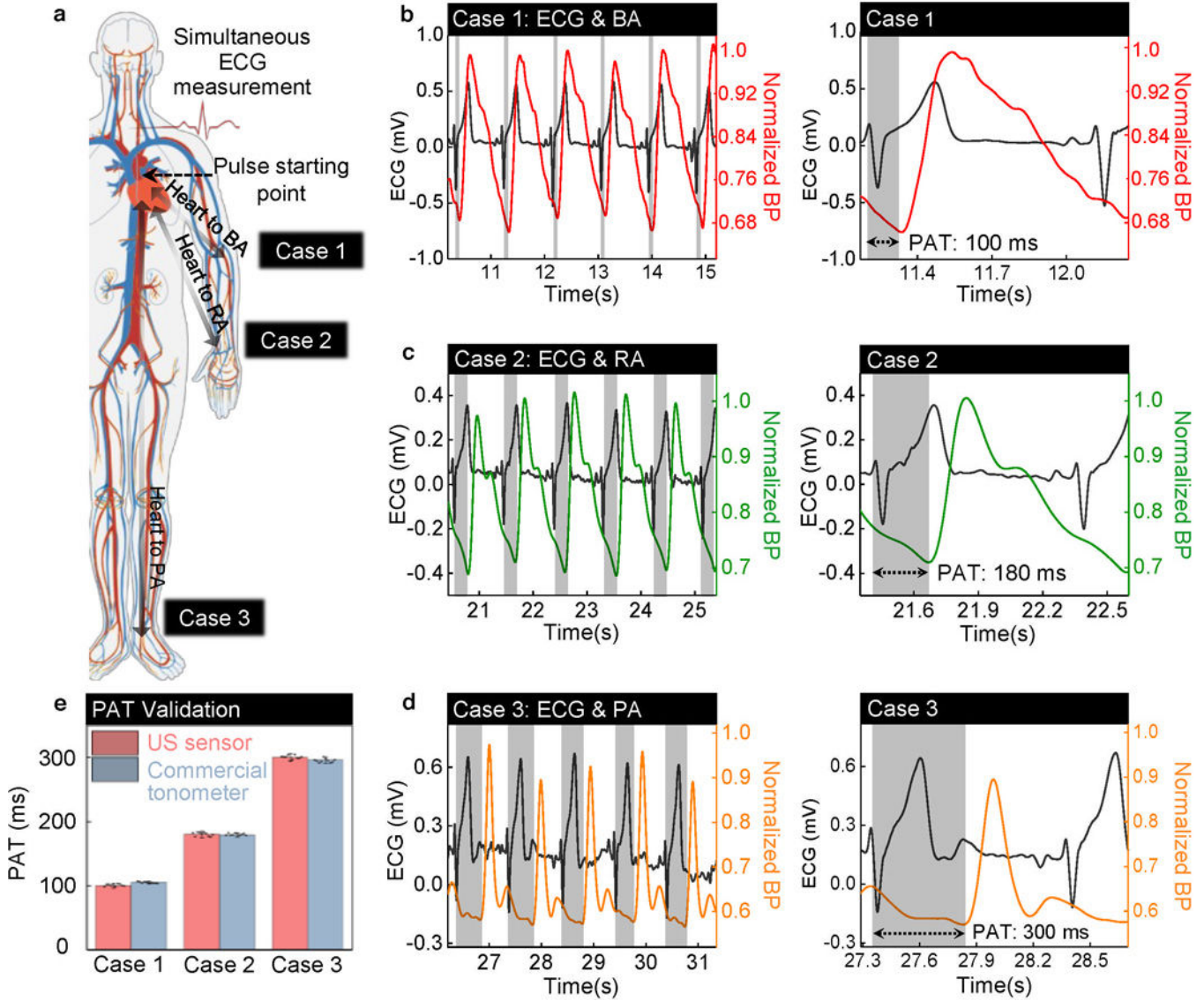
Figure | 5.

ECG correlation based PWV calculation to evaluate the arterial stiffness. **a,** Illustration of the measurement positions of the three cases from the central to the peripheral arteries, with simultaneous ECG measurements. BP waveforms are normalized based on the systolic pressure. **b,** Case 1: simultaneous measurement of ECG and BP at the BA. **c,** Case 2: simultaneous measurement of ECG and BP at the RA. **d,** Case 3: simultaneous measurement of ECG and BP at the pedal artery (Dorsalis pedis). The graphs on the right panel of **b**, **c**, and **d** show the PAT, as indicated by the grey area, for each case. **e,** PAT results compared between the conformal device and the tonometer. Dots represent all data points. Error bars represent ± s.d. (N=10).